https://doi.org/10.5194/esurf-2019-56
Preprint. Discussion started: 29 October 2019

Earth Surface Dynamics Discussions
Open Access
EGU

The role of frost cracking in local denudation of steep Alpine headwalls over millennia (Mt. Eiger, Switzerland)

David Mair[1], Alessandro Lechmann[1], Romain Delunel[1], Serdar Yeşilyurt[1], Dmitry Tikhomirov[1,2], Christof Vockenhuber[3], Marcus Christl[3], Naki Akçar[1], and Fritz Schlunegger[1]

[1]Institute of Geological Sciences, University of Bern, Bern, 3012, Switzerland
[2]Department of Geography, University of Zurich, Zurich, 8057, Switzerland
[3]Laboratory of Ion Beam Physics, ETH Zurich, Zurich, 8093, Switzerland

Correspondence to: David Mair (david.mair@geo.unibe.ch)

Abstract. Denudation of steep headwalls is driven by rock fall processes of various size and magnitude. They are sensitive to temperature changes mainly because thermo-cryogenic processes weaken bedrock through fracturing, thus pre-conditioning rock fall. However, these controls and conditions thereof on the denudation processes operating on steep headwalls have remained debated. In this study, we link new and published long-term headwall denudation rate data for the Eiger Mountain in the Central Swiss Alps with the local bedrock fabric and the temperature conditions at these sites, which depend on the insolation pattern. We then estimate the tendency of bedrock for failure through the employment of a theoretical frost cracking model, which bases on the reconstructed temperature conditions. The results show that the denudation rates are low in the upper NW headwall compared to the high rates both on the NW footwall and on the SE face, despite similar bedrock fabric conditions. For these sites, the frost cracking model predicts a large difference in cracking intensity from ice segregation where the inferred efficiency is low in the upper NW headwall, but relatively large on the lower footwall of the NW wall and on the SE flank of the Eiger. We explain this pattern by the differences in insolation and local temperature conditions. These contrasts might be enhanced by permafrost occurrence in the upper NW wall, which would further reduce cracking efficiency. Throughout the last millennium, conditions have been very similar to the present temperatures in bedrock. These data thus suggest the occurrence of large contrasts in microclimate between the NW and SE walls of the Eiger, conditioned by differences in insolation, which explain the relatively low denudation rates in the upper NW headwall of the Eiger, but the rapid denudation in the SW side and NW footwall of the Eiger where frost cracking is more efficient.

1 Introduction

Steep bedrock headwalls are a common feature of alpine landscapes. They are situated at various elevations but are especially prominent in high altitude environments. These rock surfaces experience a variety of physical and chemical processes, that result in the formation of new fractures and in the enlargement of existing weakness zones (Krautblatter and Moore, 2014; and references therein), which further promote the denudation of these headwalls. Previous research has

https://doi.org/10.5194/esurf-2019-56
Preprint. Discussion started: 29 October 2019

resulted in the generally accepted notion that among the various mechanisms leading to headwall denudation, rock fall and rockslide processes are the most important agents (e.g., Krautblatter et al., 2012; Moore et al., 2009), mainly because all loosened material is eventually removed by gravitational processes. In this context, laboratory experiments disclosed a close relationship between rock fracturing and temperature variations (e.g., Hallet et al., 1991; Murton et al., 2006). In cold and permafrost areas, a set of three different, but closely related physical processes have been proposed to cause rock to fracture (e.g., Haeberli et al., 1997; Walder and Hallet, 1985; Draebing et al., 2014). These include (i) thermal processes resulting in permafrost degradation by increased thawing (Haeberli et al., 1997; Harris et al., 2001; Krautblatter et al., 2013), (ii) thermal stresses (Collins and Stock, 2016; Eppes et al., 2016), and (iii) cryogenic processes including frost shattering by volumetric expansion during freezing (Matsuoka and Murton, 2008), and frost cracking by ice segregation (Matsuoka, 1990, 2008; Murton et al., 2006; Walder and Hallet, 1985). The effectiveness of these processes is governed by diurnal and seasonal temperature variations (Gruber et al., 2004b; Murton et al., 2006) and by temperature gradients in the bedrock (Hales and Roering, 2009; Matsuoka and Murton, 2008). Additionally the effectiveness particularly of cryogenic processes is strongly influenced by local water availability (Andersen et al., 2015; Anderson et al., 2013; Draebing et al., 2014; Sass, 2005), which conditions the formation of ice and thus the occurrence of rock falls mainly through the increase in local stresses as ice grows (Matsuoka, 2008). This requires, however, that the cooling of water and the formation of ice occurs rapidly and that the pore space is saturated with water (Walder and Hallet, 1986). These conditions limit the effective expansion to a short time window (Davidson and Nye, 1985), which rarely occurs under natural conditions as recent studies have shown (Draebing et al., 2017b). Frost cracking from ice segregation is caused by the progressive ice growth in fractures at the freezing front (Hallet et al., 1991; Matsuoka and Murton, 2008; Walder and Hallet, 1985). This process requires the supply and thus the circulation of unfrozen water in bedrock (Andersen et al., 2015; Hales and Roering, 2009; Walder and Hallet, 1985). These fracturing processes are additionally dependent on the variations in rock-type and -strength (Draebing and Krautblatter, 2012; Murton et al., 2016; Sanders et al., 2012), and they are influenced by discontinuities in the bedrock fabric (Draebing et al., 2014; Matsuoka, 2001). In particular, it has been documented that the fabric of rock exerts a strong control on rock falls where a higher fracture density in bedrock promotes the occurrence of rock falls and rock slides (e.g., Amitrano et al., 2012; Anderson, 1998; Draebing et al., 2017b; Matsuoka, 1990). Thus, in addition to climatic conditions, bedrock pre-conditioning through faulting and folding exerts a significant control on the efficiency and scale of rock fall activity (Draebing et al., 2017b; Krautblatter and Moore, 2014; Sass and Wollny, 2001). Although these relationships are well understood, little is known on how rapid denudation of bedrock headwalls has proceeded, and how denudation in these settings has responded to climatic changes particularly if longer time scales spanning millennia are considered (e.g., Gruber et al., 2004a; Krautblatter et al., 2013; Krautblatter and Moore, 2014).

Here, we combine concentrations of in-situ terrestrial cosmogenic nuclides (^{10}Be and ^{36}Cl), measured in depth profiles of a 1800 m-high vertical bedrock wall at the Eiger in the Swiss Alps (Fig. 1), with information on the bedrock fabric to quantify the long-term denudation of this mountain. We collect data from the NW and SE faces of the Eiger, which have experienced differences in insolation and thus a contrasting microclimate. We find that denudation rates are high on the SE side of the

https://doi.org/10.5194/esurf-2019-56
Preprint. Discussion started: 29 October 2019


Earth Surface Dynamics Discussions Open Access EGU

Eiger and at the foothill of the NW headwall, while denudation rates are up to four times lower on the upper part of the NW flank. We apply a simplified version of a frost cracking model to test whether the spatial pattern of denudation can be explained by the differences in microclimates around the Eiger Mountain. We find that the bedrock of the Eiger is highly fractured, which potentially promotes the occurrence of rock fall processes where dm-scale bedrock particles can be released at a high frequency. In addition, our results imply that frost cracking is effective where mean annual temperatures are slightly positive and where diurnal and annual temperature variations are large. This is particularly the case for the south side of the Eiger and also for the northern flank at its low-elevated footwall, where the denudation rates are high. We use these observations to propose that the denudation pattern of the Eiger is strongly controlled by insolation, and thus by temperature conditions.

2 Setting

2.1 Geomorphology and cosmogenic sampling sites

The Eiger Mountain (Fig. 1), which is the focus of our study, is characterized by an over-steepened, c. 1800 m-high NW face. This NW flank can be subdivided in an upper part that ranges in elevation between c. 3950 m a.s.l. and 2800 m a.s.l where the wall is nearly vertical (Fig. 1b), and in a flatter footwall segment, which continuously grades into grassland beneath an elevation of 2200 m a.s.l. On the other side, the SE flank is a several hundred-meter yet equally steep rock wall, and small active glaciers (Figs. 1a,b) border the footwall.

The denudation processes and rates operating on the Eiger Mountain have already been analyzed in a previous study, where concentrations of in-situ cosmogenic ^{36}Cl were measured in rock samples collected in four depth profiles. The sites were situated on the SE (sites EM-01 and EM-02, Fig. 1) and on the NW bedrock flanks of the Eiger (sites EW-02 and EW-03, Figs. 1, 2; Mair et al., 2019). On the NW flank, the EW-03 site is located in the footwall segment at an elevation of 2530 m.a.s.l, whereas site EW-02 is situated near the base of the upper, nearly vertical segment at an elevation of 2803 m a.s.l. On the SE flank of the Eiger, both cosmogenic sample sites are located at c. 3100 m a.s.l. The results yielded generally high denudation rates between c. 45 cm kyr^{-1} to c. 350 cm kyr^{-1} for the last centuries to millennia (Table 1). On the NW flank, denudation rates are c. 350 cm kyr^{-1} at the footwall of the Eiger (site EW-03) and c. 45 cm kyr^{-1} in the upper part of the rock wall (site EW-02). On the SW side, denudation rates range between 150 and 250 cm kyr^{-1} (sites EM-01 and EM-02). Mair et al. (2019) used these rates together with the relatively large concentration of cosmogenic ^{36}Cl at greater depths in the depth profiles to propose a model where denudation of the rock face has been accomplished by frequent, cm-scale rock fall processes together with chemical dissolution of limestone. We benefit from the results of this previous study and complement the denudation dataset with cosmogenic nuclide data of a further depth profile EW-01. This fifth section is situated at 2844 m a.s.l. at point 643168/158980 (Swiss Coordinates), near the base of the upper part of the NW face and in close proximity to site EW-02 (Table 1) of the Mair et al. (2019) study (Figs. 1a, 1b). The bedrock at sites EM-01, EM-02 and EW-02 and EW-03 mainly comprises limestone. This was also the reason why ^{36}Cl was the target cosmogenic nuclide

https://doi.org/10.5194/esurf-2019-56
Preprint. Discussion started: 29 October 2019


Earth Surface Dynamics Discussions Open Access EGU

(Mair et al., 2019). The new site EW-01, however, hosts bedrock with significant quartz content. This is the reason why for this site, we prepared samples for the analysis of in-situ ^{10}Be instead. Similar to Mair et al. (2019), bedrock samples were collected along the walls of a construction tunnel that connect the Jungfraubahnen railway tunnel with the headwall surface of the Eiger. These tunnels were used to depose material during tunnel construction between 1896 and 1905 AD. All sample sites have a local slope of $\geq 50°$, making snow cover over extended periods unlikely.

2.2 Climate and permafrost occurrence

The probability of permafrost occurrence in the Alps has been predicted based on ground surface temperature, air temperature and solar radiation. These information have been combined in a statistical model to reconstruct the Alpine-wide Permafrost Index Map (APIM) with a 30m resolution (Boeckli et al., 2012a, 2012b). For the NW face of the Eiger, the APIM data shows that all sites might be affected by permafrost. Whereas the sites EW-02 and EW-03 in the upper part of the north face show the highest tendency for permafrost occurrence (Fig. 2), the cosmogenic sampling sites on the SE facing flank are less likely to be affected by permafrost (Fig. 2).

2.3 Bedrock lithologies and fabrics

The region surrounding the Eiger is located at the geological contact between the crystalline rocks of the Aar massif, its sedimentary cover rocks and the Helvetic thrust nappes (Berger et al., 2017). The Eiger itself is mainly made up of micritic Jurassic and bioclastic Cretaceous limestone, with local chert layers and nodules, all of which were re-crystallized under lower greenschist facies conditions (c. 300°C; Mair et al., 2018; and references therin). During Alpine orogenesis, the bedrock was heavily deformed through multiple phases of folding and thrusting, which are recorded by a complex fabric in the exposed rock (Herwegh et al., 2017; Wehrens et al., 2017). At the cosmogenic sampling sites, the bedrock fabric is dominated by two generations of foliation and two sets of joints (Mair et al., 2018). The foliation that formed during the first deformation phase is oriented parallel to the sedimentary bedding and is associated with tight and isoclinal folds at the decimeter scale. The formation of this fabric was conditioned by micrometer-scale changes in sheet-silicate content during sedimentation. The second foliation is characterized by slip planes in micro shear zones, which display a large variation in the spacing between individual planes. This second foliation was considered to have formed at temperature conditions that were high enough for calcite minerals to deform in a ductile way (Mair et al., 2018). These structures are crosscut by two sets of brittle fault networks with steeply dipping fault planes. Age assignments on the formation of these structures are still a matter of debate (Mair et al., 2018).

3 Methods

We measured concentrations of cosmogenic ^{10}Be along depth profile EW-01 (Fig. 1) in order to extract information on denudation rate, exposure age and potential inheritance. The latter three variables are derived through Monte Carlo (MC)

https://doi.org/10.5194/esurf-2019-56
Preprint. Discussion started: 29 October 2019


Earth Surface Dynamics Discussions Open Access EGU

depth profile modelling techniques (Hidy et al., 2010). We then link the results of the cosmogenic nuclide analysis to the observations on the bedrock fabric, and we employ a frost cracking efficiency model to explore a potential dependency of denudation on bedrock and climate conditions. Fieldwork, including bedrock sampling, took place in winter of 2016 and summer 2017. Bedrock fabric data was collected using a geological compass and hand lenses in the field.

3.1 Analysis of *in-situ* cosmogenic ^{10}Be

3.1.1 Collection of samples, extraction of Be and AMS measurements

We collected five bedrock samples within a depth profile at site EW-01 from quartz bearing recrystallized chert layers. The material was taken from a wall of a tunnel that connects the Jungfraubahnen railway tunnel with the headwall surface. Samples were quarried with a battery saw and chisel, thereby following standard sampling protocols (Dunai and Stuart, 2009). Each sample was 5 to 10 cm thick and consisted of 1 to 1.5 kg of rock material. Concentrations of cosmogenic ^{10}Be were measured on quartz grains that were extracted from these samples. Sample preparation followed the procedure of Akçar et al. (2012) and took place at the Institute of Geological Sciences, University of Bern. ^{10}Be/^{9}Be ratios were measured by accelerator mass spectrometry (AMS) at the AMS facility at ETH Zurich, and were normalized to internal standard S2007N (Christl et al., 2013). The measured ratios were corrected with a long-term, full process blank correction of 2.44 x 10^{-15}, which amounted to relative correction between 3 and <19 %.

3.1.2 Scaling and corrections for muogenic production

In-situ cosmogenic ^{10}Be is mainly produced through spallation and muon reactions on O and Si (Gosse and Phillips, 2001). Accordingly, the production needs a scaling to geographic position and elevation, and it needs a correction for shielding from secondary cosmic ray particles (Gosse and Phillips, 2001; Lal, 1991). Production rate scaling for spallation production was done using the method of Stone (2000), which is based on the work of Lal (1991). We updated these approaches using the recalibrated reference dataset of Borchers et al. (2016) for our scaling framework. For the consideration of muogenic production, we used the parametrization scheme by Balco et al. (2008), which is based on muogenic production systematics presented by Heisinger et al. (2002a,b). The experimental fit for muogenic production of these authors, however, is known to yield in an up to ~ 40% overestimation of muogenic ^{10}Be production (Borchers et al., 2016; Braucher et al., 2003, 2013). To account for this affect, an uncertainty of 40 % was assigned on the muogenic production during the MC modelling, which is described below. We finally computed an open sky visibility on 1° azimuthal increments to account for headwall and bedrock specific geometry and shielding. This was done using a high resolution (2m) DEM provided by the Swiss Federal Office of Topography (Swisstopo) as basis. We used the combination of these constraints to calculate a total site-specific shielding factor (S_T) and apparent attenuation length ($\Lambda_{f,e}$) for spallogenic particles with the CRONUS Earth online Topographic Shielding Calculator v2.0 (Marrero et al., 2016). The shielding factor (S_T) was used to correct for both spallogenic and muogenic production, which is necessary due to the large height of the headwall (Mair et al., 2019). The

https://doi.org/10.5194/esurf-2019-56
Preprint. Discussion started: 29 October 2019

site-specific apparent attenuation length for spallogenic particles ($\Lambda_{f,e}$) was used to correct for geometric effects (Dunne et al., 1999; Gosse and Phillips, 2001). A detailed discussion of the approach can be found in the supplement of Mair et al, (2019).

3.1.3 Depth profile modelling

We used the concentrations of cosmogenic ^{10}Be in the depth profile at EW-01 to estimate the local denudation history using a Monte Carlo randomization approach (Hidy et al., 2010) and considering nuclide production at depth (Anderson et al., 1996; Braucher et al., 2009). The modelling was done with a modified Mathcad™ code of Hidy et al. (2010). A MC approach for depth profile modelling requires initial constraints on the modelled quantities, i.e., exposure age, potential inheritance and denudation rate (Hidy et al., 2010). We selected a broad range for these values in an effort not to predetermine the solution space and thus not to bias the interpretation. We thus set a constraint of (i) 75 ka on the exposure age (which is an uppermost limit given the 20 ka for the LGM), (ii) the ^{10}Be concentration of the surface sample (i.e., 1.9 x 10^4 at g^{-1}) for inherited nuclides and (iii) a maximum rate of 1500 cm kyr^{-1} on the denudation variable and a maximum of 12, 15 and 20 m for the cumulative amount of denudation for up to 75 ka. These estimates are considered as conservative values because they represent uppermost bounds for a possible exposure age, denudation rate and an inherited concentration (for a full justification see method section of Mair et al., 2019). The main purpose of running three setups for the cumulative amount of denudation is to test the independence of the model results on the initial parameter constraints on denudation, which is the case here. We note that this approach is not applicable to extract exposure ages without independent denudation constraints (Anderson et al., 1996; Hidy et al., 2010).

The modelling of TCN profiles in bedrock requires the consideration of possible inherited nuclides from previous exposure. Since such an exposure can only occur through a removal of bedrock material, such an inheritance would have been produced by muons only (due to the position of the sample at significant depth) and would follow an exponential decrease with depth (Mair et al., 2019). To account for a potential inheritance, we modelled an inherited nuclide concentration for the surface sample (C_{inh}), which we used to parametrize inheritance at depth ($C_{inh,z}$) following

$$C_{inh,z} = C_{inh} \cdot e^{(-\frac{z}{\Lambda_{inh}})}.$$

We used the value of a fitted muon attenuation length of 4852 g cm^{-2} for Λ_{inh}, which is in good agreement with published reconstructed muon attenuation lengths (Braucher et al., 2013). For rock density, we employed a uniform value of 2.68 ± 0.04 g cm^{-3} to account for the full density range between pure quartz (2.65 g cm^{-3}), the local limestone (2.68 ± 0.02 g cm^{-3} measured by Mair et al., 2019) and pure limestone (2.71 g cm^{-3}). This also includes density effects related to the occurrence of nodular chert, which was sampled for the purpose of this study. We ran the MC model until we obtained 10^5 profiles where the modeled concentrations fall within a 2σ-confidence interval of the measured ^{10}Be concentrations (which corresponds to reduced χ^2 value < 3.09). All input parameters for the MC modelling are reported in Table 2. The documentation and raw results are provided in the supplement file.

https://doi.org/10.5194/esurf-2019-56
Preprint. Discussion started: 29 October 2019

3.2 Temperature data

Fracturing of rock from frost damage and permafrost occurrence is related to local bedrock temperatures. Additional temperature parameters of interest are mean annual temperature (MAT), amplitude of annual temperature variation (dT_a) and mean amplitude of diurnal temperature variation (dT_d). We used three temperature variables as input for the frost cracking modelling, representing the conditions at sites EW-03, EW-01,-02 and EM-01,-02, respectively (Table 1). Present values for the sites EW-01 and EW-02 are based on near ground surface temperature (NGST) data at 10 cm depth by Gruber et al. (2004b) that were measured at the train stop Eigerfenster (643307, 159034, 2860 m). Data on near ground surface temperatures are also available from the train station at Eismeer (643830, 158049, 3150 m) close to our cosmogenic nuclide sampling sites EM-01 and EM-02 on the SW flank of the Eiger (Gruber et al., 2004b). We benefitted from this situation and extracted information for constraining MAT, dT_a and dT_d from the dataset spanning almost 15 years of daily averaged temperature data, available through the Swiss Permafrost Monitoring Network (PERMOS 2019; http://www.permos.ch/data.html). The MAT and dT_d values were then determined from the daily averaged temperature data, whereas dT_a was calculated from the monthly averaged values (Gruber et al., 2004b). We calculated MAT, dT_a and dT_d for the record between 2001 and 2014 AD and for the hydrological year 2002 separately. We used seven complete years of record for both the NW (Eigerfenster) and SE (Eismeer) flanks. However, the data did not cover the same years for both sites. For site EW-03 no such data was available, therefore we scaled the temperature from the Eigerfenster train station, which is the closest location for which temperature data is available, using a temperature lapse rate of -6 °C km^{-1}. In addition, for site EW-03, we applied values for dT_a and dT_d that were slightly higher than for sites EW-01,-02 because of the higher insolation due to southeast exposure. These estimated temperatures were finally used as input for the frost cracking modelling.

Past temperatures were estimated using a lake record c. 45 km farther to the west (Seebergsee). In that lake, Larocque-Tobler et al. (2012) used chironomid taxa embedded within the sediments to reconstruct a temperature history for the most recent past. These provide mean differences to the period 1961-1990 AD for the 19th century AD (0°C), the little ice age (- 0.5 °C) and the medieval climate optimum (+ 1.2 °C). We adjusted these values to the 20th century AD warming (+ 0.8 °C) and calculated MATs for the corresponding periods under the assumption of a constant diurnal and annual temperature fluctuation (Table 1).

3.3 Frost cracking modelling

Annual efficiency of frost cracking processes was computed using the mechanistic model of Andersen et al. (2015), which builds on the approach of Anderson et al. (2013), Hales and Roering (2007) and Anderson (1998). The model propagates temperature changes into the ground by solving a one-dimensional heat flow equation (Hales and Roering, 2007). The related expression considers annual surface temperature as a sinusoidal function around the MAT and dT_a and is based on a randomly superimposed sinusoidal diurnal function with an amplitude between 0 and dT_d (Andersen et al., 2015; Anderson

https://doi.org/10.5194/esurf-2019-56
Preprint. Discussion started: 29 October 2019

Earth Surface Dynamics Discussions

et al., 2013). Whereas the Andersen et al. (2015) model is capable of incorporating a sediment layer of various thicknesses atop the bedrock, we used a setup without such a layer, as we considered the local slope as too steep to accommodate a regolith layer (Table 1). The model calculates a frost cracking intensity (FCI) related to ice segregation, which is most effective where temperatures range within the so-called frost-cracking window between -8 to -3°C (Anderson, 1998; Walder and Hallet, 1985), and where water is available for ice to form (Andersen et al., 2015; Anderson et al., 2013; and references therein). The flow of water is influenced by the thermal gradient in the subsurface (Hales and Roering, 2007) and the distance to the freezing front (Anderson et al., 2013). The Andersen et al. (2015) model scales the FCI with both the thermal gradient and the occurrence of water along the path to the point of ice segregation. This is accomplished using a penalty function that integrates the flow resistance (Anderson et al., 2013) for a mixture of frozen and unfrozen bedrock (Andersen et al., 2015). We applied the material-specific standard model parameters of Andersen et al. (2015), which includes a general rock porosity of 2%. The model assumes full water saturation for the bedrock. Finally, the resulting diurnal depth-integrated $\overline{FCI}$ values are integrated over an entire year. We ran a series of models to account for variations in local temperature. We set the starting Temperature (T_0) to the site-specific MAT, and the dT_a and dT_d to the mean, minimum, maximum and the average values of 2002, respectively, and we changed these conditions upon modelling. This setup does not necessarily provide an $\overline{FCI}$ envelope, as it is based on the assumption that changes in the MAT and daily temperature amplitude also affect changes in the annual temperature amplitude in the same way, i.e., lower MATs are likewise associated with damped changes in daily and annual temperatures.

4 Results

4.1 ^{10}Be concentrations and denudation rate

The 5 rock samples have ^{10}Be concentrations (Fig. 3) ranging from 1.9 x 10^4 at g^{-1} to 0.35 x 10^4 at g^{-1} (Table 3) that decrease with depth. The standard 1σ error (0.07 x 10^4 at g^{-1} to 0.24 x 10^4 at g^{-1}; Table 3) accounts for AMS reproducibility and counting statistics, with a relative uncertainty ranging from 11 % to 69 %. The resulting concentration profile allows for MC depth profile modelling (Fig. 3) and yields values on denudation rate, exposure age and potential nuclide inheritance. The MC simulation returned 10^5 profiles where the model concentrations are within a 2σ measurement confidence interval with minima at reduced $\chi^2 = 2.32$. The MC simulation returns consistent values for inherited nuclides and denudation rate, where mean and median values are in good agreement and follow a well-defined Gaussian distribution (complete modelling results are provided in the Supplement). Thus, the MC simulation results are independent of the initial constraint on total denudation (Table 4). In detail, mean modelled inherited concentrations range from (2.4 ± 0.6) x 10^3 at g^{-1} to (2.6 ± 0.7) x 10^3 at g^{-1} ^{10}Be, accounting for 13 – 14% of the measured concentration for the surface sample. Mean denudation rate values range between (63.4 ± 13.5) cm kyr^{-1} and (64.7 ± 12.1) cm kyr^{-1}. Surface exposure ages cannot be estimated from the differing distributions for the model runs. However, the MC simulations yield agreeing minimum ages of 0.7 ka.

https://doi.org/10.5194/esurf-2019-56
Preprint. Discussion started: 29 October 2019


Earth Surface Dynamics Discussions
Open Access
EGU

4.2 Bedrock fabric

All studied sites expose bedrock with a strongly developed network of faults, fractures and foliations, especially close to the surface. The bedrock fabric at the SE flank sites EM-01, -02) is dominated by small joints that developed along the NW dipping foliation planes of both generations (S1, S3; Fig. 4). The joints are generally << 1 mm wide, but open and occasionally contain circulating water in summer, as was the case during sampling in summer of 2017 AD. The spacing between these joints varies, but generally measures between 2 and 10 cm. A second set of joints with a decimeter-wide spacing and 1 to 10 mm-wide cracks steeply dip to the SE. These joints are sometimes associated with preexisting calcite veins (Fig. 4b). The joints are generally open, but some calcite infill is also present. At the scale of an outcrop, both sets of joints are connected and regularly spaced. A third set of fractures, albeit with an irregular spacing, is found along up to several meter-broad brittle fault zones (Fig. 4c). These faults display open cracks at sub mm-scale. The spacing varies and some voids are filled with fault gauge.

A similar network of joints characterizes the sites within the NW headwall at sites EW-01, -02, -03. Joints with openings between << 1mm and 1 mm are oriented parallel to the two generations of foliations (Fig. 5), which are gently SE dipping to flat lying. A set of SE dipping open joints with widths of up to 10 mm and a spacing of 10 cm is present at all sites (Fig. 5a). We additionally found steep and headwall-parallel cracks with openings that are up to several cm wide (C2; Fig. 5d). We note that during sampling on Dec. 1st 2016, ice was present in these fractures (Fig. 5b,c).

4.3 Temperature estimates and frost-cracking modelling

The near surface ground temperatures (Table 1) reconstructed from the available daily averaged records show that the sites EW-01 and EW-02 have experienced an average MAT of -0.5 ± 0.5 °C for the full year records between 2001 and 2014 AD. This is lower than the MAT average for the SE sites (EM-01, EM-02) where the values are 1.8 ± 0.8 °C for the same period, albeit not for the exact same years (see section 3.2). On the NW flank, also at sites EW-01 and EW-02, the annual temperature amplitude of dT_a = 8.1 ± 1.3 °C is smaller compared to the dT_a = 10.7 ± 1.7 °C on the other SE side of the Eiger. A similar situation is observed for the mean diurnal temperature amplitude dT_d where the corresponding values are 6.1 ± 0.7 °C for the NW sites and 7.7 ± 0.9 °C for the SE sites. The temperature estimates for the hydrological year 2002 are similar to the mean values of the longer time period (Table 1). Temperatures for the lower NW site (EW-03) were estimated with a MAT of 1.5 ± 0.5 °C (using a constant lapse rate of , -6 °C km^{-1}), while values for dT_a of 9.0 °C and dT_d of 7.0 °C were assumed to be slightly higher than in the upper NW.

For the SE sites, the modelling of the annual frost cracking intensity ($\overline{FCI}$) returns values that range from 0.12 °C m for minimum conditions for modern dT_a, dT_d and MAT, to 0.25 °C m for the respective maximum conditions (Fig. 6, Table 5). The consideration of mean values for temperature variations and MAT returns a $\overline{FCI}$ of 0.2 °C m, which is similar to the value of 0.17 °C m that results from the model where the 2002 temperatures are considered.

https://doi.org/10.5194/esurf-2019-56
Preprint. Discussion started: 29 October 2019


Earth Surface Dynamics Discussions Open Access EGU

For site EW-03, situated at a relatively low elevation within the NW headwall, the $\overline{FCI}$ modelling yields similar results as for the sites on the other SE side of the Eiger (Fig. 6), with intensities ranging from 0.10 °C m to 0.21 °C m. The mean MAT and mean temperature amplitude model run predicts an annual frost cracking intensity of 0.16 °C m. For the sites EW-01 and EW-02, also situated on the NW headwall but at higher elevations, the modelled minimum and maximum $\overline{FCI}$ values are lower and range from 0.07 °C m to 0.12 °C m. Also at these sites, the mean MAT and mean temperature amplitude model run returns a value of 0.094 °C m, which is very close to 0.089 °C m derived for the 2002 conditions. Accordingly, the model predicts a scenario where frost cracking processes at the upper NW sites (EW-02 and EW-01) are up to 50% less effective compared to the inferred frost cracking intensities at the footwall of the NW side (site EW-03; Fig.6) and on the SE locations (EM-01, -02).

5 Discussion

5.1 Time scale of denudation rates

The concentrations of in-situ ^{10}Be along the depth profile at site EW-01 are exponentially decreasing with depth (Fig. 3a) and the relative uncertainties are relatively small (11 – 69 % for 1 σ). Accordingly, the concentration pattern can be reasonably well modelled with a Monte Carlo approach (Hidy et al., 2010). The best fitting profiles have reduced chi-square values of χ^2 = 2.3 and show a clear minimum for denudation rate and inheritance (Fig. 3b). Inherited nuclides are present at depth and at the surface, thereby accounting for 13 % to 14 % of the surface sample, and most likely derive from long-term exposure at greater depth before the current exposure period (Mair et al., 2019). The mean modelled denudation rate of 63 ± 14 cm kyr^{-1} for the 12 m total denudation model run is identical within uncertainties with mean denudation rates from the other model runs, and all mean values are very close to median and modal values (Table 4). Therefore, we consider this mean value as a robust representation of the denudation at EW-01 for at least 0.7 kyr of exposure (Braucher et al., 2009; Hidy et al., 2010). Similar to the model results of EW-02,-03, and SE-01-,-02 (Mair et al., 2019), the large inheritance at depth precludes the possibility that a large rock fall event occurred at site EW-01 during the model time interval of 1 kyr or potentially longer. Instead, we interpret that surface denudation has rather been accomplished through multiple small-scale rock fall processes were dm-large bedrock particles have been removed at a high frequency from the headwall surface. As will be discussed in the next section, we explain the small size of the particles involved in the rock fall processes by the high density of fractures and faults. However, whereas the inferred mechanisms of denudation are likely to be the same across the entire Eiger, the erosional velocities are different. In particular, the denudation rates at sites EW-03 situated on the NW footwall, and EM01,-02 on the SE flank are > 150 cm kyr $^{-1}$, and thus 4 times (45 ± 9 cm kyr^{-1}, Table 1) lower than the denudation rates at EW-02 and EW-01, situated within the upper segment of the Eiger north face, As will be discussed in section 5.3 of this paper, we explain the spatial pattern of denudation rates by differences in frost shattering processes driven by the contrasts in insolation and temperature conditions. Please note that the modelled denudation rate estimates represent

https://doi.org/10.5194/esurf-2019-56
Preprint. Discussion started: 29 October 2019

315 long-term, time-integrated values (e.g., Gosse and Phillips, 2001; Lal, 1991), most likely representative for the last millennium and possibly longer.

5.2 Preconditioning related to bedrock fabric

The rate of rock face denudation could be influenced by the bedrock fabric that affect rock failure in a complex and non-linear way (Krautblatter and Moore, 2014; Viles, 2013). Among these, fracture density and orientation has been considered
320 as the most important variables as they positively correlate with rock wall denudation (Moore et al., 2009; Rapp, 1960; Terzaghi, 1962). In the context of rock fracturing by frost weathering processes, the permeability and porosity related to faults and fractures have been identified to significantly affect the boundaries of the frost cracking window (Draebing et al., 2017b; Matsuoka, 2001; Matsuoka and Murton, 2008)) and to limit water supply within the active layer of the bedrock (Andersen et al., 2015; Anderson et al., 2013; Rode et al., 2016; Sass, 2005). At the Eiger, the bedrock fabric, in both the
325 NW and SE wall, is highly fractured along pre-existing structural weaknesses (See section 4.2). We find that fractures are developed along foliation planes (S1, S3: Figs. 3 and 4) and are thus oriented parallel to weaknesses inherited from a tectonic stress field (e.g., Fig. 4b). Beside slight differences in the orientation of the foliations, there is little difference in the bedrock fabric between the SE and NW sides. These fractures effectively allow for the disintegration of bedrock into cm- to dm-sized chips (e.g., Figs. 3a and 4a), which provides an explanation why there is no evidence in the cosmogenic dataset for the
330 occurrence of large-scale rock fall processes (e.g., Mair et al., 2019). Instead, the production of small chips is most likely achieved by frost cracking and ice segregation growth as evidenced by the ice in the bedrock cracks during sampling in December 2016 (Figs. 4b,c). The headwall parallel open joints (C2 in Fig. 5) in the NW and the large shear zones that dissect the mountain in NE – SW and SE - NW directions are suitable water pathways within the bedrock over large distances. Accordingly, the local bedrock fabric at all sites have the potential to allow for efficient bedrock weathering, and the large
335 faults and shear zones are considered as suitable pathways for water to deeply penetrate through the mountain (Fig. 5e). However, while the high density of fractures and faults provides a suitable condition for the high-frequency occurrence of small-scale rock fall processes on both sites of the Alps, this variable alone is not capable of explaining the contrasts in denudation rates between upper steep segment of the Eiger north face, and the other sites for which cosmogenic data is available. As will be elaborated in the next sections, we relate the differences in denudation rates across the Eiger to the
340 spatial pattern of frost cracking processes, which appears to be controlled by local insolation and temperature conditions.

5.3 Headwall temperature conditions and rock fracturing processes and efficiency

Variations in surface temperatures have been considered as one of the key variables driving mechanical disintegration of rock (e.g., Amitrano et al., 2012; Girard et al., 2013; Matsuoka, 2008). The instrumental record (Gruber et al., 2004b) of near ground surface temperatures (NGST; recorded at 10 cm bedrock depth) are a good proxy for temperature conditions at the
345 upper NW wall (sites EW-01,-02) and for the SE wall (sites EM-01,-02), as they have recorded actual rock temperature (Allen et al., 2009), which varies from air temperatures (Anderson, 1998). The individual sampling sites are close to the

https://doi.org/10.5194/esurf-2019-56
Preprint. Discussion started: 29 October 2019

temperature logger sites, with differences in elevation of 16 m to 57 m for the sites in the NW wall and 28 m to 50 m for the sites in the SE wall, respectively. In addition, the logger sites are characterized by similar local aspect and slope as our cosmogenic sampling sites. A potential difference in local temperature variability of up to ~ 6°C (Draebing et al., 2017a; Haberkorn et al., 2015) might arise from extended periods of sufficient snow cover. We cannot rule out the occurrence of snow cover for our cosmogenic sampling sites as snow might also accumulate on steep headwalls as the Eiger (Draebing et al., 2017a; Haberkorn et al., 2015). However, due to the similar position, aspect and slope we do not consider that the logger sites experienced different conditions than the cosmogenic nuclide sampling sites. The calculated averages of temperatures, based on 7 full hydrological years between 2001 and 2014 each, are in good agreement with the temperature values for the hydrological year 2002 (Table 1). They show a large difference in MAT (~ 2 °C), mean annual and mean diurnal amplitude (~ 1.6 °C) for the NW headwall and the SE face, with the SE face experiencing higher and more variable temperatures, despite being at ~ 300 m higher elevation. We relate this to the effect of the mountain and headwall geometry (Noetzli et al., 2007), which result in a strong insolation difference between the NW and SE walls (Fig. 7). The processes that could be affected by this variable include permafrost degradation, thermal stresses, volumetric expansion of ice from freezing and thawing, or frost cracking from ice segregation. These processes weaken the bedrock trough fracturing and thereby precondition the occurrence of rock fall. We first assess the general probability and potential effect of each process for the Eiger Mountain sites before we discuss potential controls on the denudation efficiency.

Permafrost degradation has been shown to significantly reduce rock wall stability (Gruber et al., 2004a; Haeberli et al., 1997). For the cosmogenic sampling sites, statistical permafrost models predict that permafrost is likely to have occurred at least for some time in the past (Boeckli et al., 2012b, 2012a), but is expected to be more widespread in the upper NW headwall than in the SE and the NW footwall (Fig. 2). However, the relative high temperatures (MAT = 1.8 °C; Table 1) rule out the occurrence of permafrost (Gruber et al., 2004b; Noetzli et al., 2007) at the cosmogenic sites in the SE face. Thus, degradation through permafrost alone seems an unlikely mechanism to explain the difference in denudation across the Eiger because it would affect the upper NW wall in an opposite way, which is not the case. However, the occurrence of permanently frozen rock might limit the availability of water within the rock, especially at colder temperatures (e.g., Andersen et al., 2015; Anderson et al., 2013; Draebing et al., 2017b).

Thermal stresses and subsequent expansion and contraction from daily solar temperature fluctuations can weaken bedrock and cause subcritical fracture growth (Aldred et al., 2016; Eppes et al., 2016). The occurrence of cycles where cracks open and close on a daily basis has indeed been observed in rock slopes (Draebing et al., 2017b). This mechanism has been shown to lead to progressive growth of cracks (Collins and Stock, 2016). Thermal-mechanical rock fracturing would especially affect the SE wall, as it experiences significantly more direct insolation throughout a year (Fig. 7). In a similar sense, volumetric expansion from freezing and thawing can occur under natural conditions (Matsuoka, 2008), but it is limited by ice extrusion and requires high degrees of water saturation and fast freezing (Davidson and Nye, 1985; Matsuoka and Murton, 2008). However, recent field experiments in similar environments disclosed little evidence for significant frost

https://doi.org/10.5194/esurf-2019-56
Preprint. Discussion started: 29 October 2019

cracking from volumetric expansion (Draebing et al., 2017b). Thus, we do not consider that this mechanism exerts a significant control on the denudation rates at our cosmogenic nuclide sampling sites.

Instead, we consider frost cracking from ice segregation and progressive growth of ice lenses (Walder and Hallet, 1985) as the most suitable mechanism that explains the denudation pattern we observe at the Eiger. These processes have the potential to generate large stresses up to 30 MPa in bedrock (Hallet et al., 1991). Frost cracking has been shown to be most effective within a temperature window of -3 °C to -8 °C within the rock (Hales and Roering, 2007; Walder and Hallet, 1985), but this temperature window might be affected by rock properties (Draebing et al., 2017b; Matsuoka, 2001). Theoretical modelling shows that whereas the lower boundary of the window has no significant effect on the cracking efficiency, an upper boundary of -3°C should be considered to best capture the experimental results, particularly for limestone (Hallet et al., 1991; Matsuoka, 2001). Generally, frost cracking from ice segregation has been related to two distinct temperature conditions: i) cold regions with negative MATs and ii) warm regions with positive MATs, where temperatures occasionally reach the frost cracking window (Andersen et al., 2015; Anderson et al., 2013; Delunel et al., 2010; Hales and Roering, 2007; Savi et al., 2015). For the negative MAT case, water needs to be available for continued and efficient cracking. Accordingly, in the absence of a regolith cover as a reservoir, bare bedrock might stay frozen over longer periods and therefore permafrost might reduce the cracking efficiency (Andersen et al., 2015; Draebing et al., 2017b). For the positive MAT case, frost cracking only occurs in winter, when the surface is frozen and water is available from within the bedrock (Andersen et al., 2015; Anderson et al., 2013). In winter, however, cracking intensity could be reduced through a regolith layer, which would prevent the bedrock from reaching the temperatures of the frost cracking window. Extended snow cover could increase frost cracking activity, since it has been shown to maintain the temperatures in the frost cracking window for a longer time interval, which facilitates the opening of fractures (Draebing et al., 2017b). For our Eiger sites, the lower NW and the SE sites fall within the second temperature conditions favorable for frost cracking (Table 1) and water should be available through the network of faults within the bedrock (see Section 4.2). For the upper part of the north face, MAT estimation return modern values of -0.5 °C (Table 1), which correspond to a condition for which all models predict a limited cracking efficiency from ice segregation (Andersen et al., 2015; Anderson et al., 2013; Hales and Roering, 2007). At these conditions, frost cracking occurs only at shallow depths, as the deeper rock is completely frozen without any water circulation particularly in winter. In summer, however, pore water is likely to be available, but bedrock temperatures are not reaching the FCI window. As result all modelled annual $\overline{FCI}$s predict that cracking in the SE and lower NW footwall is likely to be twice as efficient as in the upper segment of the north face (Figs. 6, and 8; Table 5). In summary, we consider that frost cracking from ice segregation, potentially affected by permafrost, and thermal stress as the most important mechanisms for the difference in rock fracturing. The effectiveness of these processes is additionally enhanced by mechanical weaknesses in the bedrock due to faults, gauges and foliations.

https://doi.org/10.5194/esurf-2019-56
Preprint. Discussion started: 29 October 2019


Earth Surface Dynamics Discussions
Open Access
EGU

5.4 Past and future conditions

The minimum exposure ages for EW-01 are 0.7 ka and 0.9 ka for EW-02 (Mair et al., 2019), which implies that the denudation rates represent integrated averages for at least these time periods. Thus, conditions during these times might have changed. Modifications in local exposure geometry and in insolation can be ruled out, which we justify through a lack of evidence for large rock fall events, which could have changed the local insolation conditions. Therefore, and because of the dependency of rock fracturing on temperatures, we consider variations in temperatures over the last millennium as the only potential variable. However, $\overline{FCI}$ calculated for mean temperatures are not exceeding the $\overline{FCI}$ estimated for maximum temperatures and the related variability during the warmest period, which is the medieval climate optimum (Fig. 6). In contrast, colder conditions, which could have prevailed during the little ice age, would have resulted in lower efficiency of frost cracking at all cosmogenic sites. However, the calculated differences in $\overline{FCI}$ between a warmer or a colder paleo-climate are lower than the contrasts in modern $\overline{FCI}$ between the upper sites in the NW headwall and the lower location on the same side of the Eiger. They are also lower than the modern $\overline{FCI}$ contrasts between the upper NW and SE headwall sites.

Temperatures are projected to increase during the 21st century up to 0.36°C per decade for the European Alps (emission scenario A1B; Gobiet et al., 2014). Mean annual air temperatures for Switzerland in 2100 AD could be between 1.9 °C and up to 5.4 °C higher than in the period 1981-2010 (emission scenarios RCP2.6 and RCP 8.5, respectively; CH2018). These projected differences in temperature are larger than the reconstructed variations for the past (Fig. 6). Such an increase in temperature could enhance the efficiency of frost cracking under similar diurnal and annual temperature amplitudes, especially in combination with permafrost degradation (Gruber and Haeberli, 2007), e.g., in the upper NW headwall. However, changes in precipitation and reduction of time spent in the frost cracking window might shift fracturing control to amplified thermal stresses, especially boosting rock fracturing on the SE face (Draebing et al., 2017b).

6 Conclusions

For our sites at the Eiger, ^{10}Be and ^{36}Cl nuclide inventories along depth profiles show that denudation on the SE wall and at the footwall of the NW flank (Fig. 8) are up to 4 times higher than the rates determined for the upper part of the NW headwall. These conditions might have prevailed for several centuries to millennia. The difference in the long-term average denudation rates particularly between the upper headwall of the Eiger north face, and the footwall and the SE side of this mountain, can be related to different efficiencies of rock fracturing processes, which strongly depend on temperature conditions (Fig. 8). Modelling indicates a strong contrast in frost cracking efficiency from ice segregation between the upper (relatively low) and lower sites on the NW wall (relatively large efficiency), but also between the upper site on the NW flank of the Eiger and the SE sites (also relatively large efficiency), which is caused by local temperature conditions. The contrast might be enhanced by permafrost in the upper NW wall, which would further reduce cracking efficiency. Furthermore, thermal stresses from differences in insolation might additionally enhance rock fracturing in the SE rock faces. Throughout

https://doi.org/10.5194/esurf-2019-56
Preprint. Discussion started: 29 October 2019

the last millennium, conditions have been very similar to the present temperatures in bedrock. Colder temperatures during the little ice age might have slightly reduced frost cracking efficiency.

Code availability

The code for the MC simulations is a modified version of the Mathcad™ file of Hidy et al. (2010), and provided in the supplement file.

Data availability

Temperature data are online available through the Swiss Permafrost Monitoring Network, PERMOS (http://dx.doi.org/10.13093/permos-2016-01). Raw MC output is provided in the supplement file.

Author contributions

DM, FS and NA designed the study; DM and AL conducted the fieldwork. DM and SY processed the samples, whereas CV and MC were responsible for the AMS measurement. DM employed the frost cracking modelling and interpreted all data with additional scientific input from DT, RD and NA, and used the Monte Carlo code updated by DT. DM prepared the manuscript and figures with contributions from all co-authors.

Competing interests

The authors declare that they have no conflict of interest.

Acknowledgements

We thankfully acknowledge the logistic support and access to the railway tunnel from the “Jungfraubahnen” Railway Company and the High Altitude Research Stations Jungfraujoch and Gornergrat (HFSJG). This research was funded by the Swiss National Science Foundation through grant No 159299 awarded to Fritz Schlunegger.

https://doi.org/10.5194/esurf-2019-56
Preprint. Discussion started: 29 October 2019

References

Akçar, N., Deline, P., Ivy-Ochs, S., Alfimov, V., Hajdas, I., Kubik, P. W., Christl, M. and Schlüchter, C.: The AD 1717 rock avalanche deposits in the upper Ferret Valley (Italy): A dating approach with cosmogenic 10Be, J. Quat. Sci., 27, 383–392, doi:10.1002/jqs.1558, 2012.

Aldred, J., Eppes, M. C., Aquino, K., Deal, R., Garbini, J., Swami, S., Tuttle, A. and Xanthos, G.: The influence of solar-induced thermal stresses on the mechanical weathering of rocks in humid mid-latitudes, Earth Surf. Process. Landforms, 41, 603–614, doi:10.1002/esp.3849, 2016.

Allen, S. K., Gruber, S. and Owens, I. F.: Exploring steep bedrock permafrost and its relationship with recent slope failures in the Southern Alps of New Zealand, Permafr. Periglac. Process., 20, 345–356, doi:10.1002/ppp.658, 2009.

Amitrano, D., Gruber, S. and Girard, L.: Evidence of frost-cracking inferred from acoustic emissions in a high-alpine rock-wall, Earth Planet. Sci. Lett., 341–344, 86–93, doi:10.1016/j.epsl.2012.06.014, 2012.

Andersen, J. L., Egholm, D. L., Knudsen, M. F., Jansen, J. D. and Nielsen, S. B.: The periglacial engine of mountain erosion - Part 1: Rates of frost cracking and frost creep, Earth Surf. Dyn., 3, 447–462, doi:10.5194/esurf-3-447-2015, 2015.

Anderson, R. S.: Near-Surface Thermal Profiles in Alpine Bedrock: Implications for the Frost Weathering of Rock, Arct. Alp. Res., 30, 362, doi:10.2307/1552008, 1998.

Anderson, R. S., Repka, J. L. and Dick, G. S.: Explicit treatment of inheritance in dating depositional surfaces using in situ 10Be and 26Al, Geology, 24, 47, doi:10.1130/0091-7613(1996)024<0047:ETOIID>2.3.CO;2, 1996.

Anderson, R. S., Anderson, S. P. and Tucker, G. E.: Rock damage and regolith transport by frost: An example of climate modulation of the geomorphology of the critical zone, Earth Surf. Process. Landforms, 38, 299–316, doi:10.1002/esp.3330, 2013.

Balco, G., Stone, J. O., Lifton, N. A. and Dunai, T. J.: A complete and easily accessible means of calculating surface exposure ages or erosion rates from 10Be and 26Al measurements, Quat. Geochronol., 3, 174–195, doi:10.1016/j.quageo.2007.12.001, 2008.

Boeckli, L., Brenning, A., Gruber, S. and Noetzli, J.: A statistical approach to modelling permafrost distribution in the European Alps or similar mountain ranges, Cryosphere, 6, 125–140, doi:10.5194/tc-6-125-2012, 2012a.

Boeckli, L., Brenning, A., Gruber, S. and Noetzli, J.: Permafrost distribution in the European Alps: Calculation and evaluation of an index map and summary statistics, Cryosphere, 6, 807–820, doi:10.5194/tc-6-807-2012, 2012b.

Borchers, B., Marrero, S., Balco, G., Caffee, M., Goehring, B., Lifton, N., Nishiizumi, K., Phillips, F., Schaefer, J. and Stone, J.: Geological calibration of spallation production rates in the CRONUS-Earth project, Quat. Geochronol., 31, 188–198, doi:10.1016/j.quageo.2015.01.009, 2016.

Braucher, R., Brown, E. T., Bourlès, D. L. and Colin, F.: In situ produced 10Be measurements at great depths: Implications for production rates by fast muons, Earth Planet. Sci. Lett., 211, 251–258, doi:10.1016/S0012-821X(03)00205-X, 2003.

Braucher, R., Del Castillo, P., Siame, L., Hidy, A. J. and Bourlés, D. L.: Determination of both exposure time and

https://doi.org/10.5194/esurf-2019-56
Preprint. Discussion started: 29 October 2019

denudation rate from an in situ-produced 10Be depth profile: A mathematical proof of uniqueness. Model sensitivity and applications to natural cases, Quat. Geochronol., 4, 56–67, doi:10.1016/j.quageo.2008.06.001, 2009.

Braucher, R., Bourlès, D., Merchel, S., Vidal Romani, J., Fernadez-Mosquera, D., Marti, K., Léanni, L., Chauvet, F., Arnold, M., Aumaître, G. and Keddadouche, K.: Determination of muon attenuation lengths in depth profiles from in situ produced cosmogenic nuclides, Nucl. Instruments Methods Phys. Res. Sect. B Beam Interact. with Mater. Atoms, 294, 484–490, doi:10.1016/j.nimb.2012.05.023, 2013.

CH2018 – Climate Scenarios for Switzerland, Technical Report, National Centre for Climate Services, Zurich, 2018.

Christl, M., Vockenhuber, C., Kubik, P. W., Wacker, L., Lachner, J., Alfimov, V. and Synal, H. A.: The ETH Zurich AMS facilities: Performance parameters and reference materials, Nucl. Instruments Methods Phys. Res. Sect. B Beam Interact. with Mater. Atoms, 294, 29–38, doi:10.1016/j.nimb.2012.03.004, 2013.

Collins, B. D. and Stock, G. M.: Rockfall triggering by cyclic thermal stressing of exfoliation fractures, Nat. Geosci., 9, 395–400, doi:10.1038/ngeo2686, 2016.

Davidson, G. P. and Nye, J. F.: A photoelastic study of ice pressure in rock cracks, Cold Reg. Sci. Technol., 11, 141–153, doi:10.1016/0165-232X(85)90013-8, 1985.

Delunel, R., van der Beek, P. A., Carcaillet, J., Bourlès, D. L. and Valla, P. G.: Frost-cracking control on catchment denudation rates: Insights from in situ produced 10Be concentrations in stream sediments (Ecrins-Pelvoux massif, French Western Alps), Earth Planet. Sci. Lett., 293, 72–83, doi:10.1016/j.epsl.2010.02.020, 2010.

Draebing, D. and Krautblatter, M.: P-wave velocity changes in freezing hard low-porosity rocks: A laboratory-based time-average model, Cryosphere, 6, 1163–1174, doi:10.5194/tc-6-1163-2012, 2012.

Draebing, D., Krautblatter, M. and Dikau, R.: Interaction of thermal and mechanical processes in steep permafrost rock walls: A conceptual approach, Geomorphology, 226, 226–235, doi:10.1016/j.geomorph.2014.08.009, 2014.

Draebing, D., Haberkorn, A., Krautblatter, M., Kenner, R. and Phillips, M.: Thermal and Mechanical Responses Resulting From Spatial and Temporal Snow Cover Variability in Permafrost Rock Slopes, Steintaelli, Swiss Alps, Permafr. Periglac. Process., 28, 140–157, doi:10.1002/ppp.1921, 2017a.

Draebing, D., Krautblatter, M. and Hoffmann, T.: Thermo-cryogenic controls of fracture kinematics in permafrost rockwalls, Geophys. Res. Lett., 44, 3535–3544, doi:10.1002/2016GL072050, 2017b.

Dunai, T. J. and Stuart, F. M.: Reporting of cosmogenic nuclide data for exposure age and erosion rate determinations, Quat. Geochronol., 4, 437–440, doi:10.1016/j.quageo.2009.04.003, 2009.

Dunne, J., Elmore, D. and Muzikar, P.: Scaling factors for the rates of production of cosmogenic nuclides for geometric shielding and attenuation at depth on sloped surfaces, Geomorphology, 27, 3–11, doi:10.1016/S0169-555X(98)00086-5, 1999.

Eppes, M. C., Magi, B., Hallet, B., Delmelle, E., Mackenzie-Helnwein, P., Warren, K. and Swami, S.: Deciphering the role of solar-induced thermal stresses in rock weathering, Bull. Geol. Soc. Am., 128, 1315–1338, doi:10.1130/B31422.1, 2016.

https://doi.org/10.5194/esurf-2019-56
Preprint. Discussion started: 29 October 2019

Fu, P. and Rich, P. M.: A geometric solar radiation model with applications in agriculture and forestry, Comput. Electron. Agric., 37, 25–35, doi:10.1016/S0168-1699(02)00115-1, 2002.

Girard, L., Gruber, S., Weber, S. and Beutel, J.: Environmental controls of frost cracking revealed through in situ acoustic emission measurements in steep bedrock, Geophys. Res. Lett., 40, 1748–1753, doi:10.1002/grl.50384, 2013.

Gobiet, A., Kotlarski, S., Beniston, M., Heinrich, G., Rajczak, J. and Stoffel, M.: 21st century climate change in the European Alps-A review, Sci. Total Environ., 493, 1138–1151, doi:10.1016/j.scitotenv.2013.07.050, 2014.

Gosse, J. C. and Phillips, F. M.: Terrestrial in situ cosmogenic nuclides: Theory and application, Quat. Sci. Rev., 20, 1475–1560, doi:10.1111/j.1755-0998.2010.02842.x, 2001.

Gruber, S. and Haeberli, W.: Permafrost in steep bedrock slopes and its temperatures-related destabilization following climate change, J. Geophys. Res. Earth Surf., 112, 1–10, doi:10.1029/2006JF000547, 2007.

Gruber, S., Hoelzle, M. and Haeberli, W.: Permafrost thaw and destabilization of Alpine rock walls in the hot summer of 2003, Geophys. Res. Lett., 31, 1–4, doi:10.1029/2004GL020051, 2004a.

Gruber, S., Hoelzle, M. and Haeberli, W.: Rock-wall temperatures in the Alps: Modelling their topographic distribution and regional differences, Permafr. Periglac. Process., 15, 299–307, doi:10.1002/ppp.501, 2004b.

Haberkorn, A., Hoelzle, M., Phillips, M. and Kenner, R.: Snow as a driving factor of rock surface temperatures in steep rough rock walls, Cold Reg. Sci. Technol., 118, 64–75, doi:10.1016/j.coldregions.2015.06.013, 2015.

Haeberli, W., Wegmann, M. and Mühll, D. V.: Slope stability problems related to glacier shrinkage and permafrost degradation in the Alps, Eclogae Geol. Helv., 90, 407–414, 1997.

Hales, T. C. and Roering, J. J.: Climatic controls on frost cracking and implications for the evolution of bedrock landscapes, J. Geophys. Res. Earth Surf., 112, 1–14, doi:10.1029/2006JF000616, 2007.

Hales, T. C. and Roering, J. J.: A frost "buzzsaw" mechanism for erosion of the eastern Southern Alps, New Zealand, Geomorphology, 107, 241–253, doi:10.1016/j.geomorph.2008.12.012, 2009.

Hallet, B., Walder, J. S. and Stubbs, C. W.: Weathering by segregation ice growth in microcracks at sustained subzero temperatures: Verification from an experimental study using acoustic emissions, Permafr. Periglac. Process., 2, 283–300, doi:10.1002/ppp.3430020404, 1991.

Harris, C., Haeberli, W., Vonder Mühll, D. and King, L.: Permafrost monitoring in the high mountains of Europe: the PACE Project in its global context, Permafr. Periglac. Process., 12, 3–11, doi:10.1002/ppp.377, 2001.

Heisinger, B., Lal, D., Jull, A. J. T., Kubik, P., Ivy-Ochs, S., Neumaier, S., Knie, K., Lazarev, V. and Nolte, E.: Production of selected cosmogenic radionuclides by muons: 1. Fast muons, Earth Planet. Sci. Lett., 200, 345–355, doi:10.1016/S0012-821X(02)00640-4, 2002a.

Heisinger, B., Lal, D., Jull, A. J. T., Kubik, P., Ivy-Ochs, S., Knie, K. and Nolte, E.: Production of selected cosmogenic radionuclides by muons: 2. Capture of negative muons, Earth Planet. Sci. Lett., 200, 357–369, doi:10.1016/S0012-821X(02)00641-6, 2002b.

Herwegh, M., Berger, A., Baumberger, R., Wehrens, P. and Kissling, E.: Large-Scale Crustal-Block-Extrusion During Late

https://doi.org/10.5194/esurf-2019-56
Preprint. Discussion started: 29 October 2019

Alpine Collision, Sci. Rep., 7, 1–10, doi:10.1038/s41598-017-00440-0, 2017.

Hidy, A. J., Gosse, J. C., Pederson, J. L., Mattern, J. P. and Finkel, R. C.: A geologically constrained Monte Carlo approach to modeling exposure ages from profiles of cosmogenic nuclides: An example from Lees Ferry, Arizona, Geochemistry, Geophys. Geosystems, 11, doi:10.1029/2010GC003084, 2010.

Krautblatter, M. and Moore, J. R.: Rock slope instability and erosion: Toward improved process understanding, Earth Surf. Process. Landforms, 39, 1273–1278, doi:10.1002/esp.3578, 2014.

Krautblatter, M., Moser, M., Schrott, L., Wolf, J. and Morche, D.: Significance of rockfall magnitude and carbonate dissolution for rock slope erosion and geomorphic work on Alpine limestone cliffs (Reintal, German Alps), Geomorphology, 167–168, 21–34, doi:10.1016/j.geomorph.2012.04.007, 2012.

Krautblatter, M., Funk, D. and Günzel, F. K.: Why permafrost rocks become unstable: A rock-ice-mechanical model in time and space, Earth Surf. Process. Landforms, 38, 876–887, doi:10.1002/esp.3374, 2013.

Lal, D.: Cosmic ray labeling of erosion surfaces: in situ nuclide production rates and erosion models, Earth Planet. Sci. Lett., 104, 424–439, doi:10.1016/0012-821X(91)90220-C, 1991.

Mair, D., Lechmann, A., Herwegh, M., Nibourel, L. and Schlunegger, F.: Linking Alpine deformation in the Aar Massif basement and its cover units - The case of the Jungfrau-Eiger mountains (Central Alps, Switzerland), Solid Earth, 9, 1099–1122, doi:10.5194/se-9-1099-2018, 2018.

Mair, D., Lechmann, A., Yesilyurt, S., Tikhomirov, D., Delunel, R., Vockenhuber, C., Akçar, N. and Schlunegger, F.: Fast long-term denudation rate of steep alpine headwalls inferred from cosmogenic 36Cl depth profiles, Sci. Rep., 9, 11023, doi:10.1038/s41598-019-46969-0, 2019.

Marrero, S. M., Phillips, F. M., Borchers, B., Lifton, N., Aumer, R. and Balco, G.: Cosmogenic nuclide systematics and the CRONUScalc program, Quat. Geochronol., 31, 160–187, doi:10.1016/j.quageo.2015.09.005, 2016.

Matsuoka, N.: The rate of bedrock weathering by frost action: Field measurements and a predictive model, Earth Surf. Process. Landforms, 15, 73–90, doi:10.1002/esp.3290150108, 1990.

Matsuoka, N.: Microgelivation versus macrogelivation: towards bridging the gap between laboratory and field frost weathering, Permafr. Periglac. Process., 12, 299–313, doi:10.1002/ppp.393, 2001.

Matsuoka, N.: Frost weathering and rockwall erosion in the southeastern Swiss Alps: Long-term (1994-2006) observations, Geomorphology, 99, 353–368, doi:10.1016/j.geomorph.2007.11.013, 2008.

Matsuoka, N. and Murton, J.: Frost weathering: recent advances and future directions, Permafr. Periglac. Process., 19, 195–210, doi:10.1002/ppp.620, 2008.

Messenzehl, K., Viles, H., Otto, J. C., Ewald, A. and Dikau, R.: Linking rock weathering, rockwall instability and rockfall supply on talus slopes in glaciated hanging valleys (Swiss Alps), Permafr. Periglac. Process., 29, 135–151, doi:10.1002/ppp.1976, 2018.

Moore, J. R., Sanders, J. W., Dietrich, W. E. and Glaser, S. D.: Influence of rock mass strength on the erosion rate of alpine cliffs, Earth Surf. Process. Landforms, 34, 1339–1352, doi:10.1002/esp.1821, 2009.

https://doi.org/10.5194/esurf-2019-56
Preprint. Discussion started: 29 October 2019

Murton, J. B., Peterson, R. and Ozouf, J. C.: Bedrock fracture by ice segregation in cold regions, Science (80-.)., 314, 1127–1129, doi:10.1126/science.1132127, 2006.

Murton, J. B., Ozouf, J. C. and Peterson, R.: Heave, settlement and fracture of chalk during physical modelling experiments with temperature cycling above and below 0 °C, Geomorphology, 270, 71–87, doi:10.1016/j.geomorph.2016.07.016, 2016.

Noetzli, J. and Gruber, S.: Transient thermal effects in Alpine permafrost, Cryosph., 3, 85–99, doi:10.5194/tc-3-85-2009, 2009.

Noetzli, J., Gruber, S., Kohl, T., Salzmann, N. and Haeberli, W.: Three-dimensional distribution and evolution of permafrost temperatures in idealized high-mountain topography, J. Geophys. Res., 112, F02S13, doi:10.1029/2006JF000545, 2007.

PERMOS 2019. PERMOS Database. Swiss Permafrost Monitoring Network, Fribourg and Davos, Switzerland. DOI:10.13093/permos-2019-01.

Rapp, A.: Recent Development of Mountain Slopes in Kärkevagge and Surroundings, Northern Scandinavia, Geogr. Ann., 42, 65, doi:10.2307/520126, 1960.

Rode, M., Schnepfleitner, H. and Sass, O.: Simulation of moisture content in alpine rockwalls during freeze–thaw events, Earth Surf. Process. Landforms, 41, 1937–1950, doi:10.1002/esp.3961, 2016.

Sanders, J. W., Cuffey, K. M., Moore, J. R., MacGregor, K. R. and Kavanaugh, J. L.: Periglacial weathering and headwall erosion in cirque glacier bergschrunds, Geology, 40, 779–782, doi:10.1130/G33330.1, 2012.

Sass, O.: Rock moisture measurements: Techniques, results, and implications for weathering, Earth Surf. Process. Landforms, 30, 359–374, doi:10.1002/esp.1214, 2005.

Sass, O. and Wollny, K.: Investigations regarding Alpine talus slopes using ground-penetrating radar (GPR) in the Bavarian Alps, Germany, Earth Surf. Process. Landforms, 26, 1071–1086, doi:10.1002/esp.254, 2001.

Savi, S., Delunel, R. and Schlunegger, F.: Efficiency of frost-cracking processes through space and time: An example from the eastern Italian Alps, Geomorphology, 232, 248–260, doi:10.1016/j.geomorph.2015.01.009, 2015.

Stone, J. O.: Air pressure and cosmogenic isotope production, J. Geophys. Res. Solid Earth, 105, 23753–23759, doi:10.1029/2000JB900181, 2000.

Terzaghi, K.: Stability of Steep Slopes on Hard Unweathered Rock, Géotechnique, 12, 251–270, doi:10.1680/geot.1962.12.4.251, 1962.

Viles, H. A.: Linking weathering and rock slope instability: Non-linear perspectives, Earth Surf. Process. Landforms, 38, 62–70, doi:10.1002/esp.3294, 2013.

Walder, J. S. and Hallet, B.: Geological Society of America Bulletin A theoretical model of the fracture of rock during freezin, GSA Bull., 96, 336–346, doi:10.1130/0016-7606(1985)96<336, 1985.

Walder, J. S. and Hallet, B.: The Physical Basis of Frost Weathering: Toward a More Fundamental and Unified Perspective, Arct. Alp. Res., 18, 27, doi:10.2307/1551211, 1986.

https://doi.org/10.5194/esurf-2019-56
Preprint. Discussion started: 29 October 2019

Wehrens, P., Baumberger, R., Berger, A. and Herwegh, M.: How is strain localized in a meta-granitoid, mid-crustal basement section? Spatial distribution of deformation in the central Aar massif (Switzerland), J. Struct. Geol., 94, 47–67, doi:10.1016/j.jsg.2016.11.004, 2017.

https://doi.org/10.5194/esurf-2019-56
Preprint. Discussion started: 29 October 2019

Earth Surface Dynamics Discussions
Open Access
EGU

635 **Figures**

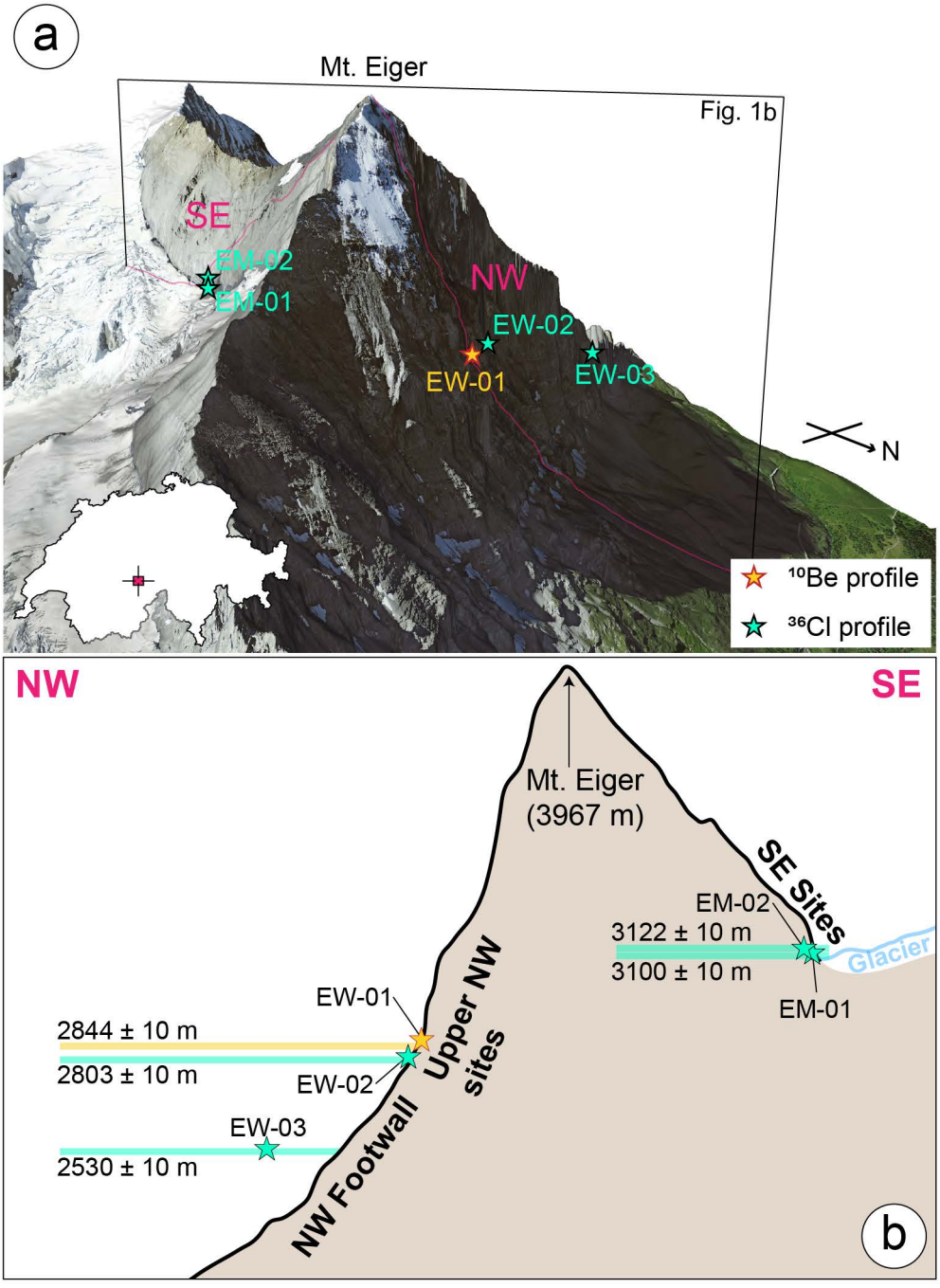

Figure 1: The Eiger Mountain in the Central Swiss Alps (insert) is characterized by steep SE and NW headwalls (a); Sampling sites for denudation rate estimations from cosmogenic nuclide analysis are indicated. (b) Schematic section along trace highlighted in panel (a); Cosmogenic sampling sites (stars) are projected into the section, and elevation of sample sites are also indicated.

https://doi.org/10.5194/esurf-2019-56
Preprint. Discussion started: 29 October 2019

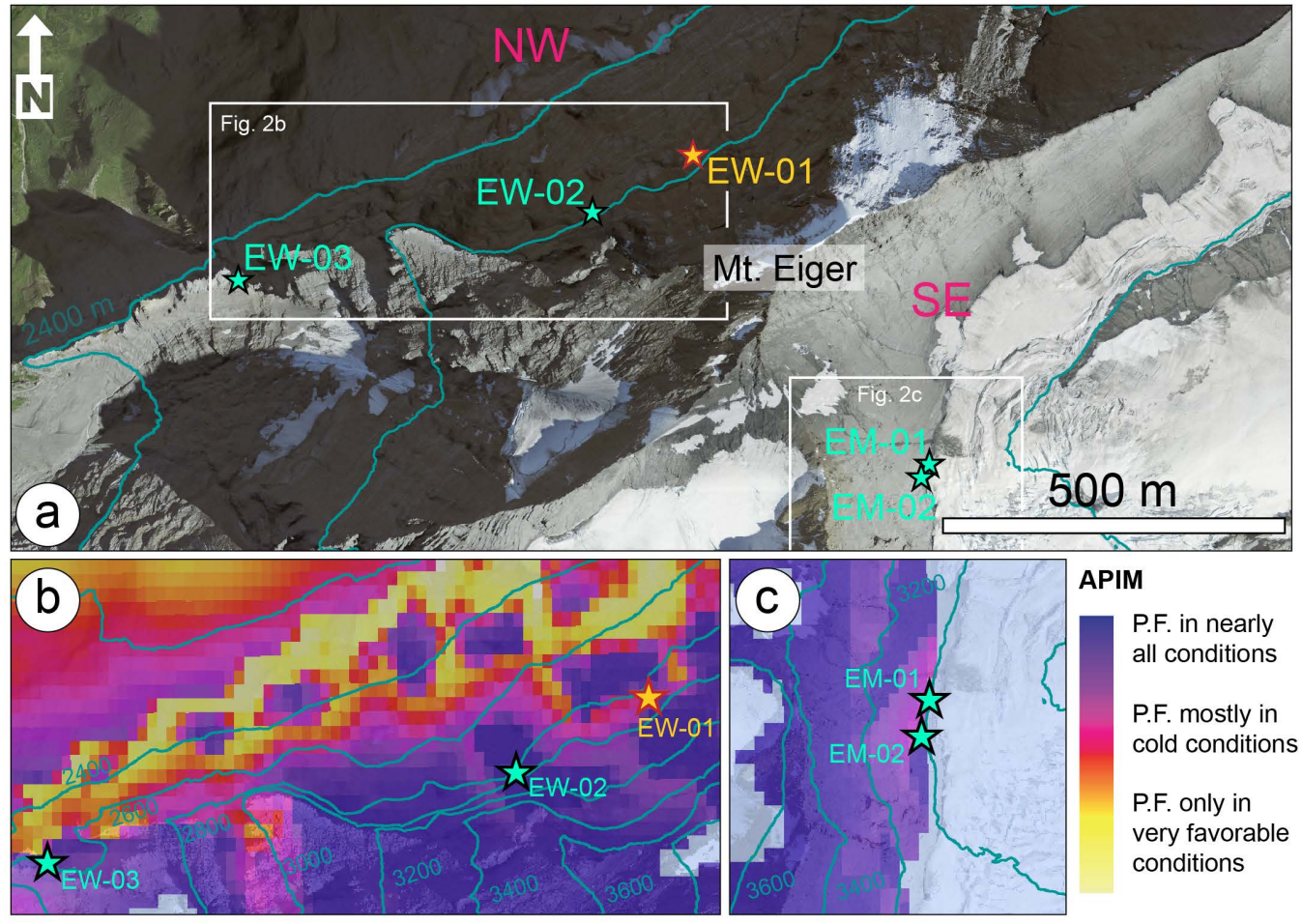

640

Figure 2: (a) Sample sites shown on a local map and with permafrost probability from the Alpine-wide Permafrost Index Map (APIM; Boeckli et al., 2012b, 2012a; b, c). Orthophoto used for the underlying hill-shaded DEM. Reproduced with permission of the federal office of topography, (Swisstopo). P.F. = permafrost.

https://doi.org/10.5194/esurf-2019-56
Preprint. Discussion started: 29 October 2019

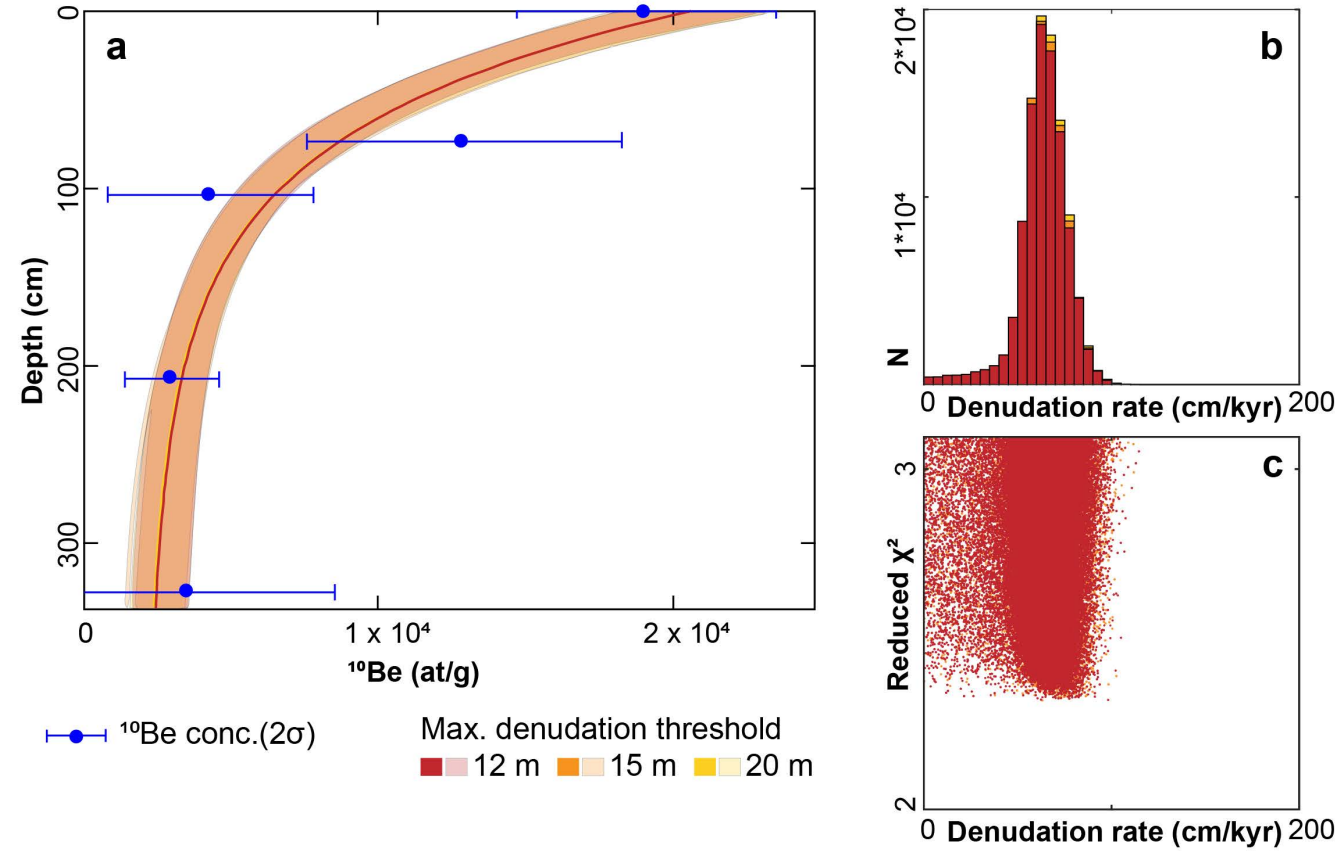

645 **Figure 3:** Results for cosmogenic ^{10}Be analysis at site EW-01. (a) Measured ^{10}Be concentrations plotted against the solution space (light colors) and the best-fit profiles. (b) Denudation rate histogram from the Monte Carlo (MC) modelling for 10^5 model profiles with corresponding reduced chi-square (χ^2) values showing (c). Different model setup results are superimposed (for discussion see text).

https://doi.org/10.5194/esurf-2019-56
Preprint. Discussion started: 29 October 2019

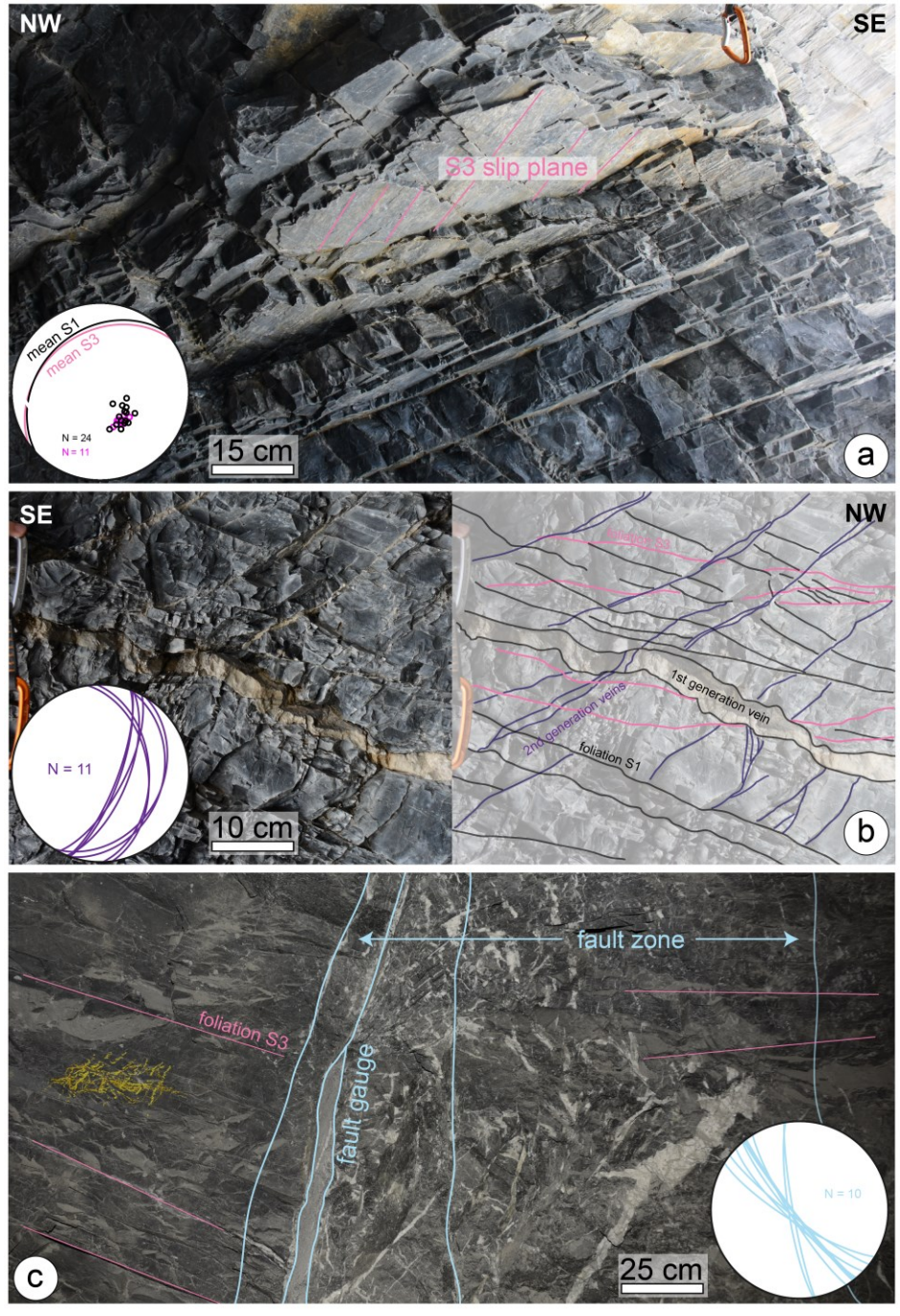

Figure 4: Bedrock fabric and discontinuity network at sample sites EM-01 and EM-02 at the SE sides. (a) Bedrock at current surface close to EM-01 highlighting the weathering paths along preexisting weaknesses. (b) Details of the bedrock fabric at site EM-02 with structural interpretation in the right panel. (c) Fault zone near the sampling sites that deeply penetrate the Eiger (based on Appendix image from Mair et al., 2018). Structural orientation data partly based on Mair et al. (2018).

https://doi.org/10.5194/esurf-2019-56
Preprint. Discussion started: 29 October 2019

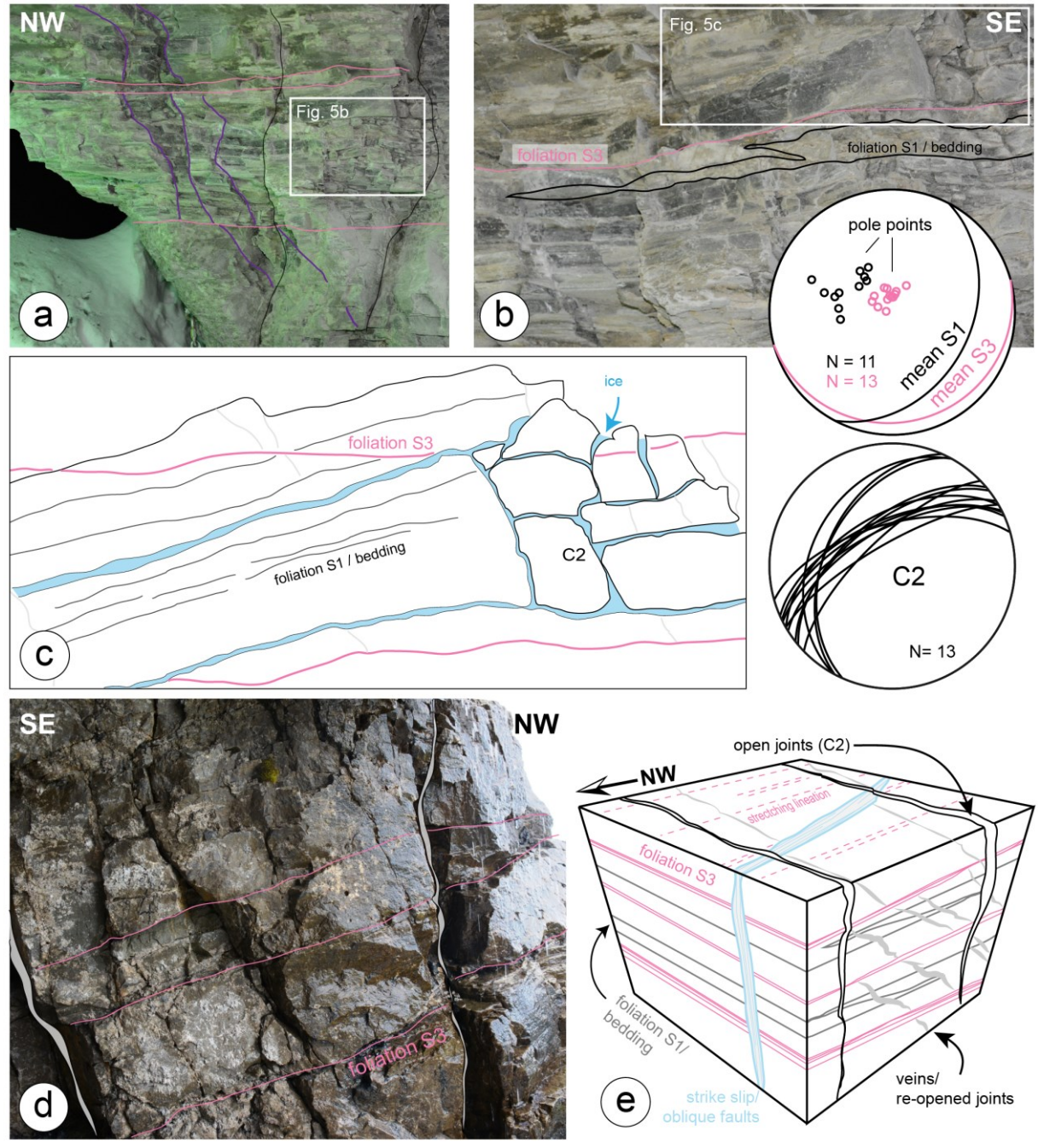

Figure 5: Bedrock fabric from cosmogenic sites within the NW face, at site EW-02 (a). (b,c) Details with ice lenses present during sampling on Dec. 1st 2016 AD, highlighting the relation of fractures with the pre-existing structures. (d) Structures at sampling sites EW-01. (e) Bedrock discontinuities relevant for bedrock fracturing, synthesized for the NW headwall.

https://doi.org/10.5194/esurf-2019-56
Preprint. Discussion started: 29 October 2019

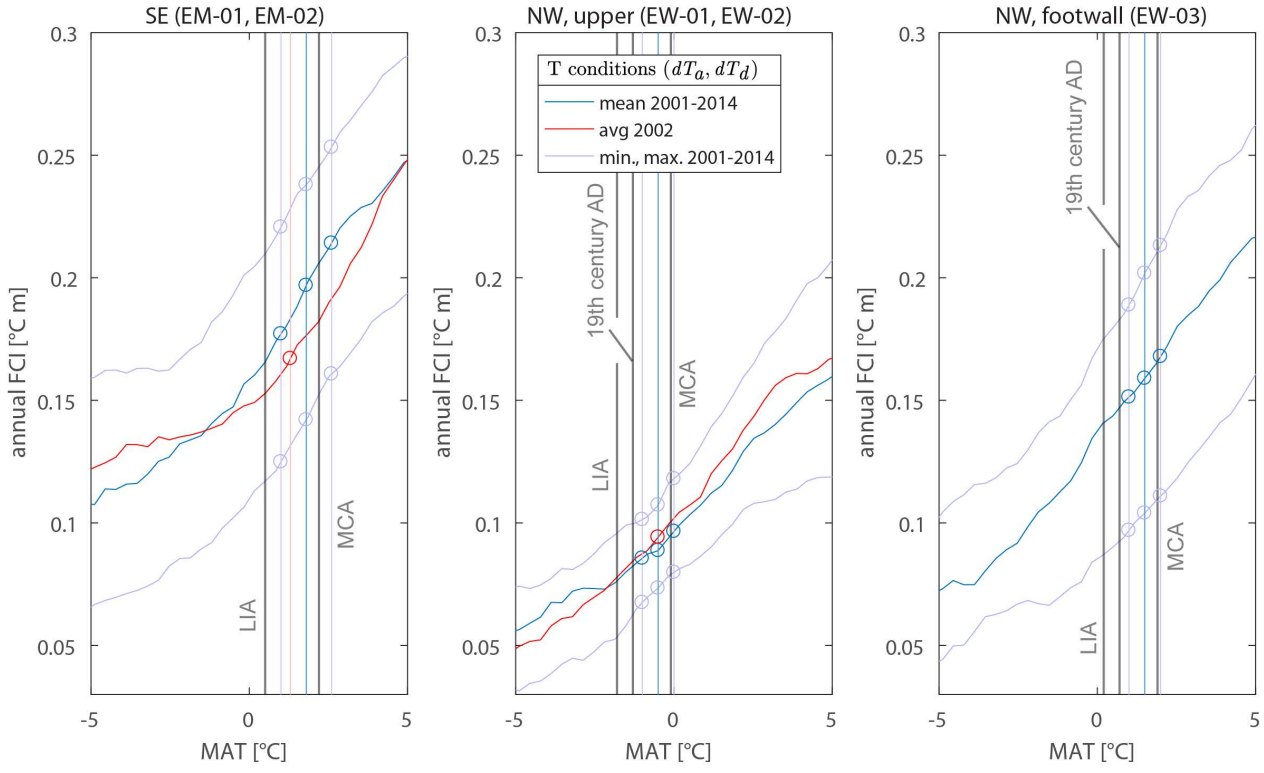

Figure 6: Modelled annual frost cracking intensity ($\overline{FCI}$) for the individual sites and the different thermal regimes. For the site-specific model run conditions (min, max, mean and 2002) see Table 1 and Section 3.2. Resulting $\overline{FCI}$ values for the indicated circles are presented in Table 4. MAT = mean annual temperature, LIA = little ice age, MCA = medieval climate optimum.

https://doi.org/10.5194/esurf-2019-56
Preprint. Discussion started: 29 October 2019

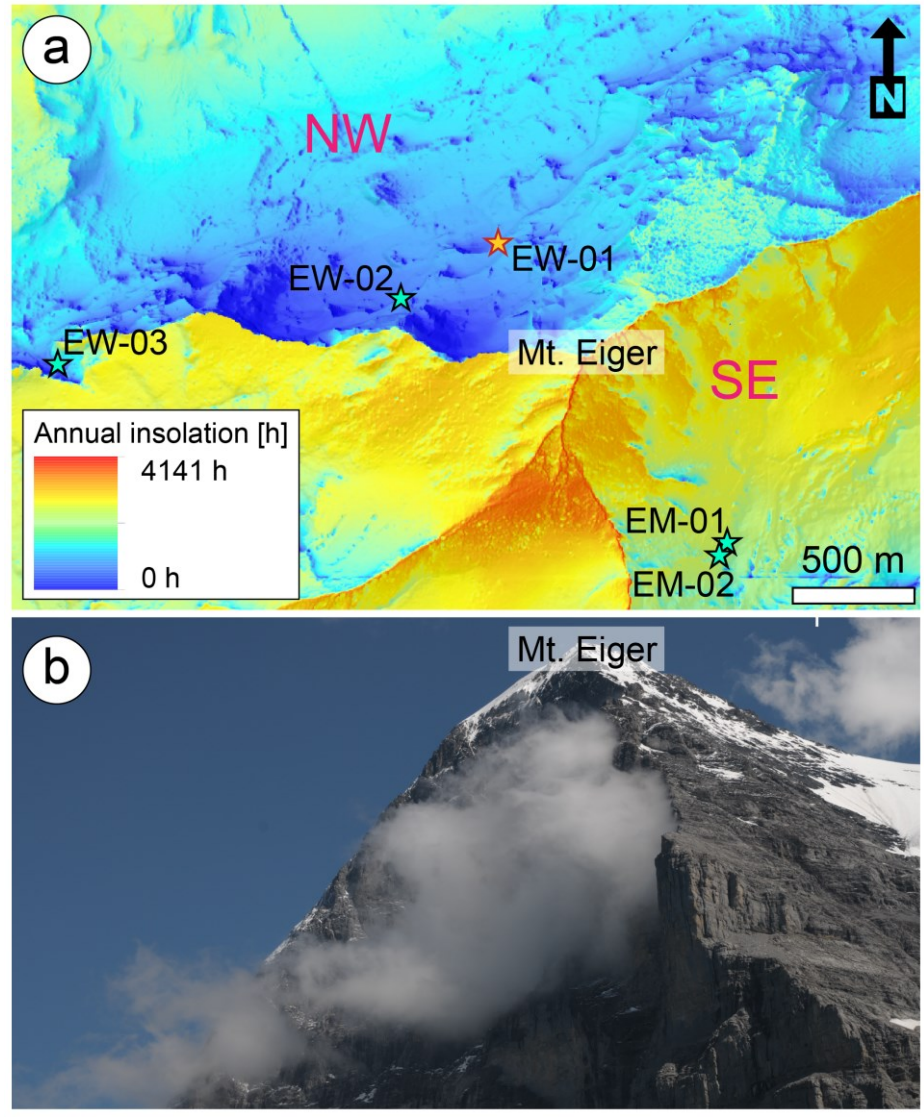

Figure 7: Differences in local temperature conditions between the NW and the SE face. (a) Potential annual solar insolation in hours over a year, calculated using the hemispherical viewshed algorithm included in ESRIs ArcGIS™ (Fu and Rich, 2002). (b) Field photograph of the NW wall, taken in the summer of 2017 AD, with local clouds illustrating the potential difference in microclimatic conditions.

https://doi.org/10.5194/esurf-2019-56
Preprint. Discussion started: 29 October 2019

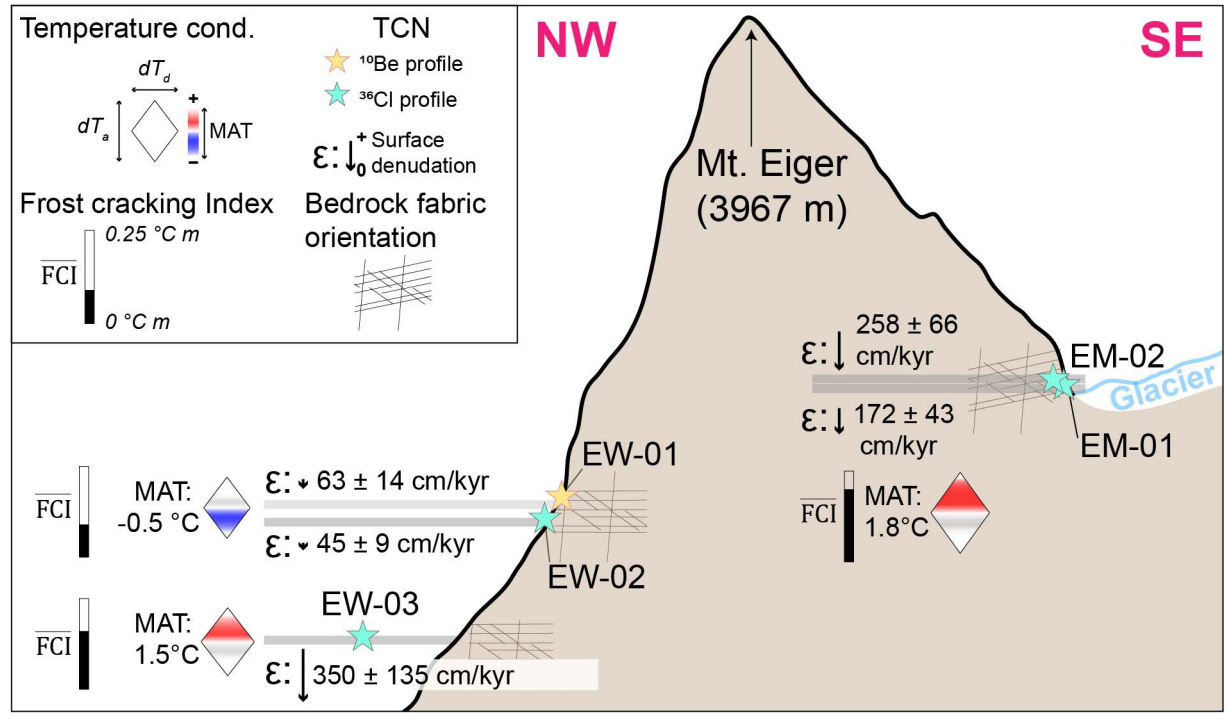

Figure 8: Schematic section (for trace see Fig. 1) with main findings indicated. MAT = mean annual temperature, $\overline{FCI}$ = annual frost cracking intensity index, ε = denudation rate. $\overline{FCI}$ symbols represent mean modern temperature conditions (Table 4), MAT symbols represent mean modern temperature conditions color-coded with symbol size representing mean annual, diurnal amplitude (Table 1); see text for discussion.

https://doi.org/10.5194/esurf-2019-56
Preprint. Discussion started: 29 October 2019

Earth Surface Dynamics Discussions
Open Access
EGU

Tables

TCN Site	EW-01	EW-02	EW-03	EM-01	EM-02
Elevation [m]	2844	2803	2530	3100	3122
Slope [°]	50	53	83	75	75
Aspect [°]	370	298	7	96	111
Denudation rate [cm kyr^{-1}]	63.4 ± 13.5	45.4 ± 9[a]	350.1 ± 135[a]	172.0 ± 43[a]	258 ± 66[a]
	Upper NW		Lower NW	SE	
Temperature regime	**NGST 2002**				
MAT [° C]	-0.5		n/a	1.3	
dT_a [° C]	8.1		n/a	10.3	
dT_d [° C]	5.8		n/a	7.8	
	NGST Present (2001 - 2014)				
MAT [° C]	-0.5 ± 0.5		(1.5 ± 0.5)[ǂ]	1.8 ± 0.8	
dT_a [° C]	8.1 ± 1.3		(9.0 ± 1.5)[*]	10.7 ± 1.7	
dT_d [° C]	6.1 ± 0.7		(7.0 ± 1)[*]	7.7 ± 0.9	
	19th century AD				
MAT [° C]	-1.3		0.7	1.0	
	LIA				
MAT [° C]	-1.8		0.2	0.5	
	MCA				
MAT [° C]	-0.1		1.9	2.2	

Table 1: Study site parameters and reconstructed temperature values. NGST sites from Gruber et al. (2004b); temperature data available at http://www.permos.ch/data.html (PERMOS 2019). For used record, see method section. [a] data from Mair et al. (2018), [ǂ] scaled from the Eigerfenster site (Gruber et al., 2004b), [*] values assumed (see section 3.2 for details). TCN = terrestrial cosmogenic nuclide, NGST = near ground surface temperatures at a depth of 10cm, LIA = little ice age, MCA = medieval climate optimum, MAT = mean annual temperature, dT_a = amplitude of annual temperature variation, dT_d = mean amplitude of diurnal variation; n/a = not available.

https://doi.org/10.5194/esurf-2019-56
Preprint. Discussion started: 29 October 2019

Earth Surface Dynamics Discussions
Open Access
EGU

Parameter	Value
Elevation [m]	2844
Latitude [degree]	46.58070
Longitude [degree]	8.00181
Slope [°]	50
Strike [°]	227.2
Shielding factor S_T	0.55
Cover correction	1
Reference production rate [at g^{-1} a^{-1}]	4.01
Local spall. production rate [at g^{-1} a^{-1}]	19.84 ± 1.98
Uncertainty of ^{10}Be half-life [%]	5
Depth of muon fit [m]	30
Density [g cm^{-3}]	2.68 ± 0.04
Error on muogenic production rate [%]	40
Apparent attenuation length $\Lambda_{f,e}$ [g cm^{-2}]	153.2 ± 15.3
χ^2 cut-off	3.09
Min. age [a]	0
Max. age [a]	75000
Min. denudation rate [cm kyr^{-1}]	0
Max. denudation rate [cm kyr^{-1}]	1500
Min. total denudation [cm]	0
Max. total denudation [cm]	1200, 1500, 2000
Min. inheritance [at g^{-1}]	0
Max. inheritance [at g^{-1}]	19012

Table 2: Input parameters for the modified Monte Carlo (MC) simulation code of Hidy et al. (2010).

https://doi.org/10.5194/esurf-2019-56
Preprint. Discussion started: 29 October 2019

Earth Surface Dynamics Discussions
Open Access
EGU

Sample	Depth [cm]	Dissolved Qtz [g]	^{10}Be spike [mg]	^{10}Be/^{9}Be [10^{-14}]	^{10}Be measured concentration [10^{4} at/g]
EW-01-1	0.0	50.01830	0.1991	7.39 ± 0.8	1.90 ± 0.21
EW-01-3	73.3	50.07070	0.1988	5.08 ± 0.96	1.28 ± 0.26
EW-01-4	103.5	44.37640	0.1988	1.66 ± 0.56	4.23 ± 0.17
EW-01-5	207.0	50.12830	0.1991	1.35 ± 0.27	2.92 ± 0.07
EW-01-6	327.8	50.20810	0.1990	1.56 ± 0.9	3.48 ± 0.24

680 **Table 3:** Measured ^{10}Be/^{9}Be ratios and ^{10}Be concentrations for samples of depth profile EW-01. ^{10}Be concentrations were adjusted using a measured long-term average blank ratio of 2.44 x 10^{-15}, amounting to corrections of between 3 and <19 %.

https://doi.org/10.5194/esurf-2019-56
Preprint. Discussion started: 29 October 2019

Earth Surface Dynamics Discussions
Open Access
EGU

	Age [ka]	**ε [cm/kyr]**	**Inh. [10^3 at/g]**	**Age [ka]**	**ε [cm/kyr]**	**Inh. [10^3 at/g]**	**Age [ka]**	**ε [cm/kyr]**	**Inh. [10^3 at/g]**
	12 m max. denudation			15 m max. denudation			20 m max. denudation		
MEAN	9.3	63.4	2.6	11.6	64.0	2.5	15.4	64.7	2.4
STD	5.4	13.5	0.7	6.8	12.8	0.7	9.1	12.1	0.8
MEDIAN	9.0	64.3	2.6	11.3	64.6	2.6	15.1	65.0	2.4
MODE	1.1	64.3	3.0	1.2	63.0	3.0	1.2	62.8	2.0
Min	0.7	0.0	0.0	0.7	0.0	0.0	0.7	0.1	0.0
lowest χ^2	6.8	98.5	2.2	21.1	63.4	1.9	21.1	63.4	1.9
Max	29.9	114.9	4.5	37.3	113.3	4.7	54.3	114.9	4.9

Table 4: Result statistics for Monte Carlo (MC) depth profile modelling of profile EW-01.

https://doi.org/10.5194/esurf-2019-56
Preprint. Discussion started: 29 October 2019

Earth Surface Dynamics Discussions
Open Access
EGU

T regime	Model setups (dT_a and dT_d)	$\overline{FCI}$ min. MAT [°C m]	$\overline{FCI}$ mean MAT [°C m]	$\overline{FCI}$ max. MAT [°C m]	$\overline{FCI}$ 2002 MAT [°C m]
SE	Min 2001- 2014	0.12	0.14	0.16	n/a
	Mean 2001- 2014	0.18	0.20	0.21	0.17
	Max 2001- 2014	0.22	0.24	0.25	n/a
NW	Min 2001- 2014	0.07	0.07	0.08	n/a
	Mean 2001- 2014	0.09	0.09	0.10	0.09
	Max 2001- 2014	0.10	0.11	0.12	n/a
Lower NW (EW-03)	Min 2001- 2014	0.10	0.10	0.11	n/a
	Mean 2001- 2014	0.15	0.16	0.17	n/a
	Max 2001- 2014	0.19	0.20	0.21	n/a

Table 5: Selected annually integrated frost cracking efficiencies ($\overline{FCI}$) for the studied temperature regimes, and the different model runs with the respective mean annual temperatures (MAT). T = temperature, n/a = not available.